Reevaluating the electrical impact of atomic carbon impurities in MoS_2

James Ramsey,[1] Faiza Alhamed,[1,2] Alexander G. Christison,[1] J. P. Goss,[1] P. R. Briddon,[1] and M. J. Rayson[1]
[1]*School of Mathematics, Statistics and Physics, Newcastle University, Newcastle upon Tyne, NE1 7RU, United Kingdom*
[2]*College of Science and Arts, Najran University, Najran 66462, Saudi Arabia*

(Received 26 June 2025; revised 19 February 2026; accepted 26 March 2026; published 23 April 2026)

Transition metal dichalcogenides, a family of two-dimensional compounds, are of interest for a range of technological applications. MoS_2, the most researched member of this family, is hexagonal, from which monolayers may be isolated. Under ambient conditions and during growth/processing, contamination by impurities can occur, of which carbon is significant due to its presence in the common growth techniques. We have performed extensive computational investigations of carbon point defects, examining substitutional and interstitial locations. Previously unreported thermodynamically stable configurations: Fourfold coordinated monocarbon and dicarbon substitutions of Mo, and a complex of carbon substitution of sulfur bound to interstitial sulfur have been identified. We find no evidence to support recent assertions that carbon defects are responsible for electrical doping of MoS_2, finding all energetically favorable forms have only deep charge transition levels and would act as carrier traps. To aid in the unambiguous identification of carbon defects, we present electronic and vibrational data for comparison with spectroscopy.

DOI: 10.1103/wfjb-8dd2

I. INTRODUCTION

Since the experimental isolation of monolayer graphene [1], 2D van der Waals-layered materials have been a promising area of research interest due to their electrical and mechanical properties. Combining this with their atomic length scales, these materials are positioned as strong candidates to overcome the scaling limits [2] of magnetic data storage devices [3], photovoltaic cells [4], and conventional silicon-based electronics [5–7]. The zero band gap limits graphene's application, whereas semiconducting transition metal dichalcogenides (TMDs) exhibit suitable band gaps in the range 1.1–2.0 eV [8], tunable by the number of layers; the MoS_2 band gap varies monotonically with thickness between 1.23 eV (indirect) [9] in bulk, to 1.9 eV [10–13] for the monolayer (direct). MoS_2 also benefits from a room-temperature carrier mobility $>200\ \mathrm{cm}^2/(\mathrm{V\,s})$ [14], comparable to Si, an in-plane Young's modulus exceeding that of steel [15], and a solar photon absorption an order of magnitude greater than Si or GaAs [16] due to its high refractive index [17].

Presently, the performance of TMD-based optoelectronic devices does not meet theoretical predictions. For example, photovoltaic cells deliver power conversion efficiencies lower than the theoretical maximum [17] by factors of 5 or greater, even for state-of-the-art devices [18–20]. The main reasons for underperformance include device-level factors such as Fermi-level pinning [21], contamination or corrugation at TMD-TMD interfaces [19] and inefficient exciton separation [18] due to charge-carrier trapping at point defects [22,23]. Characterizing contamination and point defects is therefore crucial.

Native point defects are dominant over impurities in MoS_2. In Mo-rich (S-lean) growth conditions, literature data [24–29] consistently indicate the sulfur vacancy, V_S, is pervasive due to its energetically favorable formation energy, E_f, at 1.5 eV [24,25] in combination with its sizable ($\gtrapprox$2 eV) diffusion barrier [30] for all stable charge states [28], rendering it immobile under ambient, processing, and growth conditions. In Mo-lean (S-rich) conditions, the sulfur interstitial, S_i, presents as another stable center with low E_f (0.9 eV [29,31]), which is immobile at room temperature due to its appreciable diffusion barrier (1.7 eV [28,30]).

As for impurities, it has been suggested that carbon is unintentionally substituted into the material from low purity Mo precursors during chemical vapor deposition (CVD) [32]. It is also proposed that carbon is codeposited during metal-organic CVD [33] from pyrolysis of the metal organic [34] or organosulfur [35] precursors, followed by subsequent substitution into the host material under atmospheric conditions [34]. Carbon has also been reported to form nanometer-scale clusters, particularly at the sites of sulfur vacancies [36]. Carbon is therefore a notable contaminant to understand the properties of as-grown MoS_2, particularly for scalable applications.

Carbon is also considered a prime candidate for a source of *n*-type conductivity [14,33,37–45] in field-effect transistors constructed of as-grown MoS_2. However, the precise origin of the conductivity is disputed. Different authors suggest Cl or Br substitution for S [39], substitution of Re for Mo [28], hydrogenated native defects [46], and carbon [33,37], specifically interstitial impurities [37], could be potential causes. In particular, Ref. [37] attributed *n*-type conductivity to carbon by experimental observation of a concurrent *p*-to-*n*-type

Published by the American Physical Society under the terms of the Creative Commons Attribution 4.0 International license. Further distribution of this work must maintain attribution to the author(s) and the published article's title, journal citation, and DOI.

transition with increasing carbon deposition time. This is identified by a relative shift of the Fermi level away from the valence band edge in angle-resolved photon-emission spectroscopy. A similar dependence of nanometer-scale defect concentration (notably not atomic scale) on carbon deposition time is also identified. These observations were sought to be explained using first-principles calculations, noting that some carbon interstitial structures shift the Fermi energy towards the conduction band relative to the pure material [37]. In the candidate structures, an additional carbon atom is located above a Mo-site, approximately in-plane with three sulfur neighbors, forming fourfold coordination (C_i^{Mo}, Fig. 1(f), Refs. [37,47–50]), or alternatively with C bridging between a Mo and a S atom in a twofold coordination [C_i^{Bridge}, Fig. 1(g)]. However, such an assignment is rendered problematic when noting that these structures are not the equilibrium structure [51], with C lying in the Mo-layer coordinated to three Mo (C_i^{MoC}, Fig. 1(h), Ref. [51]) being more energetically stable. In fact, several more recent publications [32,47,49,50] omit this low-energy configuration from their analysis. This highlights a need to establish more definitively the equilibrium behavior of carbon interstitials and their properties.

Ultimately, the impact an impurity has upon electrical conductivity must correspond to a mechanism for the release or capture of free carriers. If carbon has a direct role in electrical doping, this should be both evident from a thermally-accessible charge transition level and relate to thermodynamically favorable arrangements.

In this paper, we present the results of a detailed investigation of carbon point-defects in monolayer MoS_2 using density functional theory (DFT). We report geometries, energetic stabilities, electronic structures, magnetic states, and vibrational modes, providing routes to experimental observation. Our focus is upon a robust evaluation of the relative energetics of different forms of carbon contamination, and to challenge the conclusions that simple centers, especially interstitial carbon, can be responsible for electrical doping. The inclusion of spectroscopically observable properties, both from the band structure and from the vibrational modes, is with the aim of providing direct routes to experimental identification of the microstructures of carbon defects in MoS_2.

II. COMPUTATIONAL METHOD

Calculations were performed using the AIMPRO [52,53] DFT modeling software package, within the PBE generalized gradient approximation (GGA) [54], and the Grimme-D2 van der Waals (vdW) correction [55]. It is well understood that GGA functionals tend to underestimate electronic properties such as the band-gap energy. However, previous studies [56,57] have shown that hybrid functionals result in slightly deeper calculated donor and acceptor levels than their generalized gradient and local functional counterparts for centers similar to those explored in this study. We note that there are differences between the PBE and HSE06 trap depths, but in no case for this study does the trend in increasing depth of donor or acceptor levels qualitatively impact the conclusions we draw. vdW corrections are typically only important for interlayer interactions of multilayer systems. We include this correction for consistency with other studies and have assessed the choice of parametrization for test systems. For example, varying the implementation to Grimme-D3 results in less than 1 meV/atom difference in the bulk 2H-MoS_2 interlayer binding energy, and less than 0.1 eV difference for formation energies of a carbon-containing point-defect in monolayer MoS_2. We conclude that the details of the vdW correction do not materially impact any of our computed values. Pseudopotentials [58,59] were utilized with 4, 14, and 6 electrons in the valence sets for C, Mo, and S, respectively, eliminating core electrons. Kohn-Sham functions were expanded using atom-centered, independent Gaussian orbital functions [60], using *s*-, *p*-, and *d*-type functions with four widths amounting to 40 functions/atom. For sample calculations, increasing the number of basis functions to five widths (50 functions) affects relative energies by 2 meV or less, indicating that the basis is well suited to the determination of defect energies. Hamiltonian matrix-elements were generated using a plane-wave expansion [52] of the charge-density and Kohn-Sham potential with a minimum of 150 Ha cut-off, yielding well converged total energies (better than 0.1 meV/atom) with respect to this parameter.

For all calculations except those for minimum energy paths (see below), defects were introduced to a base-supercell comprised from 300 atoms corresponding to 10×10 primitive unit cells. Integration over the Brillouin-zone is by Monkhorst-Pack sampling [61]; the primitive pristine monolayer sampling is 15×15, with all nonprimitive cells modeled with equal or greater sampling densities. To determine an estimate of the impact of the choice of sampling scheme, the total energy of pristine MoS_2 was determined using a range of sampling densities. We find that using the 15×15 mesh results in absolute total energies that are converged to $\ll 1$ meV/atom.

Equilibrium structures are obtained by optimizing geometries until the maximum final force is less than 1 mHa/bohr. Using this approach, the in-plane lattice constant of pristine monolayer MoS_2 is found to be 3.20 Å, in agreement with previous reports [27,29]. The out of plane constant is 15 Å to minimize interactions between periodic images, resulting in formation energies converged to $\mathcal{O}$(meV) compared to a 53 Å constant. The Mo-S bond lengths and electronic band gap of monolayer MoS_2 were found to be 2.42 Å and 1.64 eV, respectively, also in agreement with previous calculations (2.4 Å [62,63] and 1.7 eV [46,64]).

Formation energies [65] of system X in charge state q, $E_f(X,q)$, are obtained using $E_f(X,q) = E_t(X,q) - \sum_i n_i\mu_i + q\mu_e + E_{\text{corr}}$, where $E_t(X,q)$ is the total energy, n_i is the number of atoms of species i with chemical potential μ_i in the pristine system of identical supercell dimension, μ_e is the electron chemical potential, and E_{corr} is an electrostatic corrective term for charged systems in periodic boundary conditions. E_{corr} is calculated for charged systems following the FNV scheme [65–67] and has been applied utilizing the `sxdefectalign2d` implementation [67]. Neutral formation energies calculated in 10×10 cells are converged upon those at the extrapolated dilute limit to $\mathcal{O}$(10 meV). The convergence of formation energies of charged systems is less well-defined due to the necessity of correcting for the periodic boundary condition and vacuum effects (i.e., the `sxdefectlign2d` approach), but the values are still

TABLE I. Symmetry, coordination, and selected geometric parameters of uncharged C-containing point defects in monolayer MoS_2. Distances are in angstroms and angles are quoted to the nearest degree. For comparison, for pristine MoS_2, the calculated Mo–S distance is 2.42 Å and ∠Mo-S-Mo is 83°. Geometric quantities for systems with net charge differ only modestly from the neutral case, included in Ref. [74].

Defect	Sym.	Fig. 1	C coord.	Geometric Quantities	
C_{Mo}	C_{3v}	(a)	3	C–S ∠SCS	1.74 119
C_{Mo}	C_{1h}	(b)	4	C–S ∠SCS	1.85 93, 108, 109 × 2, 118 × 2
$(C_2)_{Mo}$	D_{3h}	(c)	4	C–S, C–C ∠SCS, ∠CCS	1.83, 1.57 106, 113
C_S	C_{3v}	(d)	3	C–Mo ∠MoCMo	2.02 104
C_i^S	C_{3v}	(e)	1	C–S ∠SCS, ∠MoSMo	1.68 130, 84
C_i^{Mo}	C_{3v}	(f)	4	C–S, C–Mo ∠CSMo, ∠SCMo	1.81, 2.06 118, 99
C_i^{Bridge}	C_1	(g)	2	C–S, C–Mo ∠SCMo	1.64, 2.14 116
C_i^{MoC}	D_{3h}	(h)	3	C–Mo ∠MoCMo	2.03 120
$(C_S - S_i)^{HS}$	C_{3v}	(i)	4	C–Mo, C–S ∠MoCMo, ∠SCMo	2.20, 1.64 91, 124
$(C_S - S_i)^{LS}$	C_{1h}	(j)	4	C–Mo, C–S ∠MoCMo, ∠MoCS, ∠CSMo	(2.12 × 2, 2.23), 1.66 (93 × 2, 97), (132 × 2, 86), 56

broadly independent of cell size varying by $\mathcal{O}(100$ meV). Taking the equilibrium phase as pure monolayer MoS_2 which must be stable relative to its elemental components, $\mu_{Mo} = E_t(MoS_2) - 2\mu_S$, with μ_{Mo} bounded by the energy per atom of body-centered cubic Mo (Mo-rich limit) and μ_S the energy per atom of bulk cyclo-octosulfur (Mo-lean limit). We define the relative chemical potential of Mo as $\Delta\mu_{Mo} = 0$ for Mo-lean conditions, and the carbon atomic chemical potential is taken to be the energy per atom of pure diamond. The formation energy of $V_S(1-)$ and its $(0/-)$ charge transition level have been calculated at 3.2 eV (S-lean condition, $\mu_e = E_{VBM}$) and $E_{VBM} + 1.5$ eV, respectively, in good agreement with previous studies [26,28,29,68].

Carbon adsorption energies, E_{ad}, are formation energies obtained with μ_C being the energy of a free carbon atom, E_C. The ground-state energy of a carbon atom is challenging because the many-body wavefunctions are not well represented by the single determinental formulation in DFT. To accommodate this issue, the experimental cohesive energy of diamond ($E_{coh} = -7.43$ eV/atom [69,70]) is used to infer the atomic energy, i.e. $E_C = E_{diamond} - E_{coh}$, where $E_{diamond}$ is the calculated energy per atom of diamond. Based upon this estimate of the carbon energy, our calculated values obtained by fractional filling of the $2p$-states for a single atom represent overestimates by 0.9 and 2.5 eV for spin-polarized and spin-averaged configurations, respectively. Hence, utilizing diamond's cohesive energy mitigates the impact that the choice of the atomic carbon energy has upon the estimated adsorption energies.

Minimum energy paths were calculated using the climbing nudged-elastic-band method [71,72] utilizing supercells of 4×4 or 6×6 primitive cells and a minimum of 9 images. The saddle-points were allowed to climb after the third iteration. The larger cell is used for dissociation of a sulfur interstitial from a complex with C_S to allow for the separation of the component parts. Convergence tests on selected reactions indicate activation energies determined in the smaller cell are uncertain to 10s of meV.

Finally, local vibrational modes were modeled within the harmonic approximation, with dynamical-matrix elements found using a finite difference approximation for the second derivatives of the energy with respect to displacement [73]. We confine the analysis to wave numbers above the one-phonon maximum that represent local modes characteristic of the defect and internal bonding.

III. RESULTS

We have examined carbon substitutions at the Mo or S sites and as an interstitial. To provide for reaction energies, we have also modeled monovacancies and sulfur-interstitial defects. We report here geometric, energetic, electronic, and vibrational data, starting with the defect geometries.

A. Defect geometries

Figure 1 illustrates carbon defects with the associated structural parameters listed in Table I. Pristine MoS_2 is illustrated in Figs. 1(k)–1(l) for geometrical comparison with each impurity.

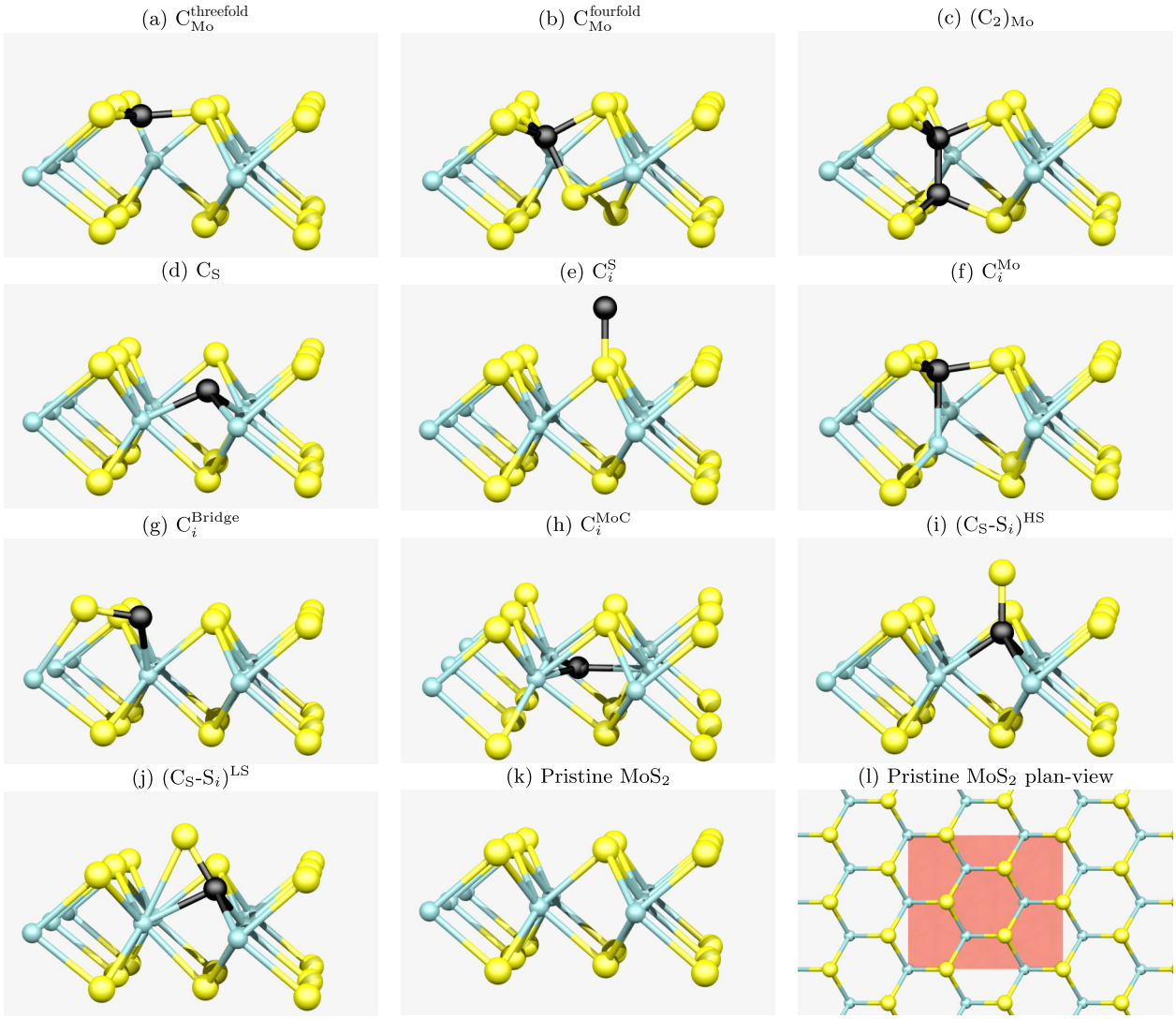


FIG. 1. Schematic structures of carbon defects in monolayer MoS_2. (a) and (b) show the three- and fourfold coordinated configurations of C_{Mo}, (c) the dicarbon substitution, $(C_2)_{Mo}$ (d) C_S, and (e)–(h) show C_i in four configurations where the carbon is above S, above Mo, bridging between the Mo and S sites, and in the Mo plane, respectively. (i) and (j) illustrate $C_S - S_i$ in high (HS) and low symmetry (LS) configurations. Blue, yellow, and black spheres represent Mo, S, and C, respectively. (k) illustrates pristine MoS_2 for comparison to each defect center, and (l) shows in plan view the depicted material section (shaded area) for each of the structures. Depictions of the centers from plan-view are available in the supplemental information [74].

Substitution of Mo by C, C_{Mo}, directly onto the Mo site results in a D_{3h} point-group symmetry and sixfold effective coordination of C ($C_{Mo}^{sixfold}$). The optimized Mo–S distance is 2.29 Å, and we note the C–Mo distances of 3.23 Å are much greater than the 2.18 Å bond length in γ-MoC [75]. However, $C_{Mo}^{sixfold}$ is not the equilibrium structure, but rather a local energy maximum. Previous studies [32] suggest C_{Mo} is threefold-coordinated [$C_{Mo}^{threefold}$ Fig. 1(a)], arising from C displacement from the Mo site along [0001], rendering three S sites under-coordinated. $C_{Mo}^{threefold}$ is 2.6 eV lower in energy than $C_{Mo}^{sixfold}$, with C–S bond lengths of 1.74 Å, suggesting C–S is sp^2 hybridized by its similarity to typical C–S bond lengths in organic compounds such as the trithiocarbonate anion, $(CS_3)^{2-}$. In addition to the geometry, both the charge density and Kohn-Sham eigenfunctions support the description of the bonding as a covalent sp^2 arrangement (see Ref. [74]); there is a build-up of charge density between C and its three neighbors, and there are occupied σ- and π-bonding states present within the valence band. On the basis of the orbitals, the C–S bond-order lies between 1 and 2, consistent with the bond lengths. Both $C_{Mo}^{sixfold}$ and $C_{Mo}^{threefold}$ energetically favor a spin-triplet electronic configuration.

Our findings are in line with the literature [32], but we find a C_{1h}-symmetry fourfold coordinated arrangement 0.6 eV lower still in energy [$C_{Mo}^{fourfold}$, Fig. 1(b)]. Considering the six S neighbors of $C_{Mo}^{sixfold}$ to be in two groups of three on either side of the Mo plane, the structure of $C_{Mo}^{fourfold}$ can be understood as carbon forming bonds with one set of three (as in $C_{Mo}^{threefold}$), with the fourth C–S bond forming with one S atom in the other group. Although not constrained by its C_{1h} symmetry, we find the four C–S bond lengths at 1.85 Å (Table I) are the same length to within 0.5 pm, suggesting that all four bonds are of

the same type and are consistent in length with the C-S sp^3 bond in ethanthiol, CH_3CH_2SH. This inference is supported by the charge density, which is qualitatively the same for all four C–S bonds. Additionally, the Kohn-Sham functions (see Ref. [74] for isosurface illustrations) show that for the fourfold coordination, the gap states cannot be described exclusively as relating to the undercoordinated S atoms, tempting though this might be following chemical principles. Rather, the gap states result from linear combinations of p orbitals on these two atoms with bonding combinations of orbitals involving the carbon and nearby Mo atoms, with the under-coordinated sites not being particularly dominant. It is instructive to note that this is different from the behavior seen for V_{Mo}, which *does* possess gap states dominated by contributions from the unsaturated S sites. It is the higher-energy levels of V_{Mo} that most closely resemble the gap states of $C_{Mo}^{fourfold}$. Indeed, spatial distribution across under coordinated sulfur atoms and nearby 4d orbitals on nearby Mo atoms also characterizes the gap states of the threefold bonded arrangement, resembling the empty states of V_{Mo}.

Both $C_{Mo}^{threefold}$ and $C_{Mo}^{fourfold}$ contain undercoordinated S sites, suggesting that placing C in both S layers may also be favorable. We have modeled this dicarbon center, $(C_2)_{Mo}$, the optimized structure being shown in Fig. 1(c). Both carbon atoms are fourfold coordinated and the equilibrium structure retains a high symmetry (D_{3h}). The fact that the C–C bond is 1.57 Å, alongside the approximate-tetrahedral arrangement, localized tetrahedral bonding combinations of atomic orbitals in the Kohn-Sham states, and the accumulation of charge density between the carbon atoms (see Ref. [74]) are all consistent with sp^3 bonding.

Substitution for the sulfur site, C_S [Fig. 1(d)], also results in a high-symmetry configuration, with the threefold coordination of carbon. Our findings are in agreement with the literature [32,37,47]. The C–Mo bond lengths are 2.02 Å, much greater than the C–S bond lengths of C_{Mo}, but only slightly shorter than the C–Mo bond length in γ-MoC.

Finally, we turn to C_i, which is indistinguishable from an adatom due to the all-surface nature of 2D materials. We find the energies of C_i^S, C_i^{Mo} and C_i^{Bridge} [Figs. 1(e)–1(g)] to be 0.9, 0.4, and 0.5 eV respectively higher than C_i^{MoC} [Fig. 1(h)], and therefore agree with previous modeling [51] that C_i^{MoC} is the equilibrium form of C_i of those arrangements previously studied. We also note that geometry and energy depend somewhat upon the effective spin; the arrangements depicted in C_i^S and C_i^{Mo} favor the spin-triplet configuration by 0.6 and 0.3 eV relative to spin-singlets, whereas C_i^{Bridge} and C_i^{MoC} both favor the spin-singlet.

However, we challenge the view that C_i in any form is anything other than a metastable system. We find C_i^{MoC} displaces an S to form C_S bound to a sulfur interstitial, $C_S - S_i$, as illustrated in Figs. 1(i) and 1(j). These two structures correspond to spin-triplet and spin-singlet electronic configurations, respectively, which we find to be indistinguishable in total energy. $C_S - S_i$ is around 1.7 eV lower in energy than the equilibrium form of C_i^{MoC}. One might ask the question as to why $C_S - S_i$ is more energetically favorable than C_i^{MoC}. As will be shown below, one might take the lower-lying occupied band-gap state of C_i^{MoC} than $C_S - S_i$ as favoring the former,

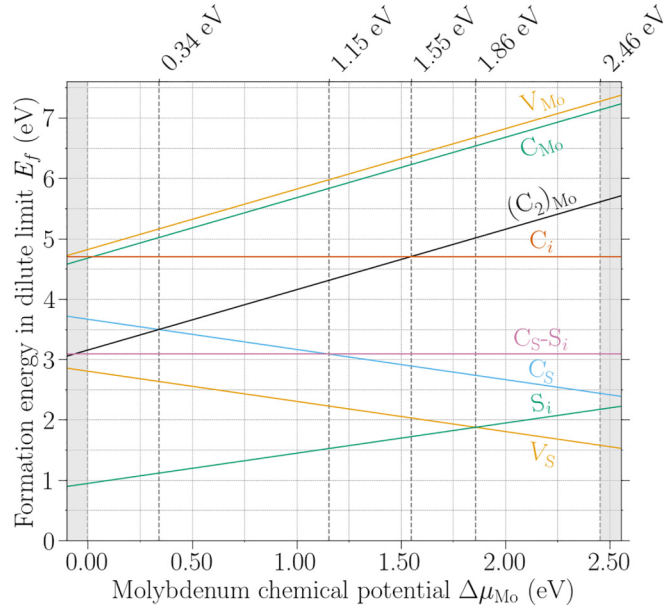


FIG. 2. $E_f(\Delta\mu_{Mo})$ for C-containing and native defects in monolayer MoS_2. $\Delta\mu_{Mo}$ is 0 eV and 2.46 eV for Mo-lean and Mo-rich limits. Dashed vertical lines highlight where E_f for pairs of defects are equal. Energies are based upon equilibrium forms in each case. Formation energies that are independent of μ_{Mo} conserve the stoichiometry of the host material.

but one must exercise caution in such an interpretation. The one-electron term in the total energy involves *all* occupied bands, and we note that the total one-electron contribution to the total energies favors $C_S - S_i$, indicating that states in the valence band are responsible for the stabilization. Even this should be viewed with caution, as the one-electron term is only part of the energy difference. We surmise that the stabilization of $C_S - S_i$ may be thought of as a combination of the lower strain and the formation of a strong C = S double bond (Table I) in $C_S - S_i$. The bonding inference from the geometry is supported by identification of σ_s, σ_s^*, σ_p, and π_p, orbitals within the range of occupied valence-band states, with π_p^* orbitals lying in the band gap containing two electrons (see Ref. [74]). This amounts to a net bond order of 2 in this case. This stabilization of the kick-out of a sulfur atom tends to mitigate against the proposal that C_i will be present in high concentrations in any form. In this case, it is difficult to see how interstitial carbon can be responsible for the n-type behavior [37].

B. Energetics

In order to directly compare between C-containing centers of different compositions, one might consider formation energy, including underlying materials conditions (Mo- and S-rich conditions) as described in Sec. II.

Figure 2 shows a plot of neutral-charge $E_f(\Delta\mu_{Mo})$ and Table II lists the corresponding values. The data obtained are in line with the consensus in the literature (Sec. I) that V_S and S_i are relatively low energy point defects in Mo-rich and S-rich limits, respectively. The energies of C-containing centers are influenced by the choice of μ_C (Sec. II), and these values

TABLE II. $E_f(\Delta\mu_{Mo})$ and heats of reaction, ΔH, for selected formation processes in the neutral charge state. Energies are quoted to the nearest 0.1 eV.

Product	E_f	Reaction + ΔH
C_{Mo}	$4.7 + \Delta\mu_{Mo}$	$V_{Mo} + C_i \rightarrow C_{Mo} + 4.8$
C_S	$3.7 - \Delta\mu_{Mo}/2$	$V_S + C_i \rightarrow C_S + 3.8$
$(C_2)_{Mo}$	$3.2 + \Delta\mu_{Mo}$	$C_{Mo} + C_i \rightarrow (C_2)_{Mo} + 6.2$
$C_S - S_i$	3.1	$C_i^{MoC} \rightarrow C_S - S_i + 1.7$
$C_S - S_i$	3.1	$C_S + S_i \rightarrow C_S - S_i + 1.5$
C_i^{MoC}	4.7	–
V_{Mo}	$4.8 + \Delta\mu_{Mo}$	–
V_S	$2.8 - \Delta\mu_{Mo}/2$	–
S_i	$0.9 + \Delta\mu_{Mo}/2$	–

should be compared with those of V_S and S_i with attention to this.

Of the carbon-containing centers, in the Mo-lean limit $C_S - S_i$, $(C_2)_{Mo}$ and C_S are most favorable and, therefore, expected to be dominant under equilibrium conditions. C_{Mo} is comparatively high in formation energy, but remains significant as a potential precursor of $(C_2)_{Mo}$. For Mo-rich conditions, C_S and $C_S - S_i$ are most energetically favorable. Our estimate of $E_f(C_S)$ is in close agreement with the literature [37], providing additional support to our computational approach. We note that the formation energies of the substitutions mirror those of the vacancies, with $E_f(C_{Mo})$ within 0.1 eV of $E_f(V_{Mo})$, and although $E_f(C_S)$ is higher than $E_f(V_S)$, the difference is less than 1 eV.

The relative energetic importance of different carbon centers may be crudely approximated using Boltzmann statistics, guided by typical growth temperatures [76–78]. Solubilities can be estimated using $[X] \sim g\exp(E_f/k_BT)$, where g is the site density, so that $[V_S] \sim [S]\exp(-E_f(V_S)/k_BT)$ yields $[V_S]/[S] \sim 10^{-8}$ at 700 °C in S-lean conditions. Since V_S is more energetically favorable than other centers investigated, equilibrium concentrations of carbon defects would be expected to be lower.

It is also insightful to evaluate the adhesion of adatoms to the surface. The adsorption energies, E_{ad}, of C_i in various geometries are presented in Table III alongside relevant literature data. As noted in Sec. II, the reference energy of a free carbon atom is not trivial to obtain directly using DFT. A naïve approach of obtaining the energy of an atom by simulating a single atom in a large periodic cell would populate the $2p$ orbitals equally. For carbon, this means each state is effectively populated by a third of an electron in each of the six orbitals and spin combinations. This is strictly not a many-body solution to the atom, but rather a weighted average over several many-body configurations. As such, the fractional occupation of the $2p$ orbitals will by construction, lead to an overestimate of the atom energy, E_C, and thus systematically overestimate the energy released upon adsorption, E_{ad}. It seems likely that overestimates in the atomic energy will be a significant contribution to the >2.0 eV spread of E_{ad} indicated in Table III. Based upon our calculations. where we have estimated the reference energies in both ways, these large sources of uncertainty in the adsorption energy are an order of magnitude larger than other considerations such as cell size. For the purpose of the comparison with the literature, the high energy C_i^{ν} form is included (carbon approximately in-plane with sulfur but not above molybdenum, see supplemental information [74]), to demonstrate the relatively large range of adsorption energies quoted in the literature, supporting our conclusion that the apparent disparities are due to different treatments of the free atom.

TABLE III. Adsorption energies, E_{ad}, for various carbon interstitial sites calculated based upon different estimates of carbon atom energies, E_C. For E_{ad}^{coh}, E_C is inferred from the cohesive energy of diamond (Sec. II). E_{ad}^0 and E_{ad}^1 are obtained using E_C as the calculated energies of a free carbon atom in a spin singlet and spin triplet configuration, respectively, neglecting multiplet effects. Energies in eV.

				Literature values				
	E_{ad}^{coh}	E_{ad}^0	E_{ad}^1	[32]	[49]	[51]	[48]	[47]
C_i^{MoC}	2.7	5.2	3.6			3.3		
C_i^{Mo}	2.3	4.8	3.3	4.7	4.3	2.7	2.5	3.4
C_i^{S}	1.7	4.2	2.7	3.8				2.8
C_i^{ν}	1.0	3.4	1.9	3.3				2.5

Using the empirically corrected atom energy, E_{ad}^{coh}, the adsorption of C onto MoS_2 is exothermic (Table III), qualitatively consistent with the literature [32,47–49,51], but quantitatively our predicted values are significantly lower. Subsequent desorption of C adatoms is therefore more likely than previously suggested, although it would remain less energetically favorable than chemically reacting with the MoS_2 to produce $C_S - S_i$.

E_{ad} has also been calculated for S_i. Using the cohesive energy approach based upon cyclo-octosulfur [79], the adsorption of S_i onto MoS_2, or C_S to form $C_S - S_i$, are estimated to be 1.9 and 3.4 eV, respectively. The latter value suggests that adsorption of a C atom followed by displacement of sulfur is unlikely to result in subsequent desorption of the sulfur interstitial.

Next, we consider the reaction energetics as a guide to thermal stability, utilizing calculated heats of reaction and energy barriers. Five reactions key to the incorporation of carbon in MoS_2 are listed in Table II, all of which are found to be exothermic.

Several of these reactions involve the diffusion of C_i. Its minimum energy diffusion barrier is via the C_i^{Mo} site and is estimated at 1.1 eV, which is competitive in comparison with S_i diffusion calculated at 1.8 eV (in agreement with [28,30]). For processes driven by the addition of interstitial species, one can imagine two chains emerging, incrementally increasing thermodynamic stability: $V_{Mo} \xrightarrow{C_i} C_{Mo} \xrightarrow{C_i} (C_2)_{Mo}$ and $V_S \xrightarrow{C_i} C_S \xrightarrow{S_i} C_S - S_i$. Formation of $(C_2)_{Mo}$, C_S and $C_S - S_i$ during growth under Mo-lean conditions may be possible by this incremental capture of interstitials, as each step is exothermic.

Of particular significance is the rearrangement of $C_i \rightarrow C_S - S_i$. For all configurations we have studied with the exception of C_i^{MoC}, the barriers to rearrangement are all sufficiently small ($\lesssim 0.7$ eV) to expect rapid completion of the

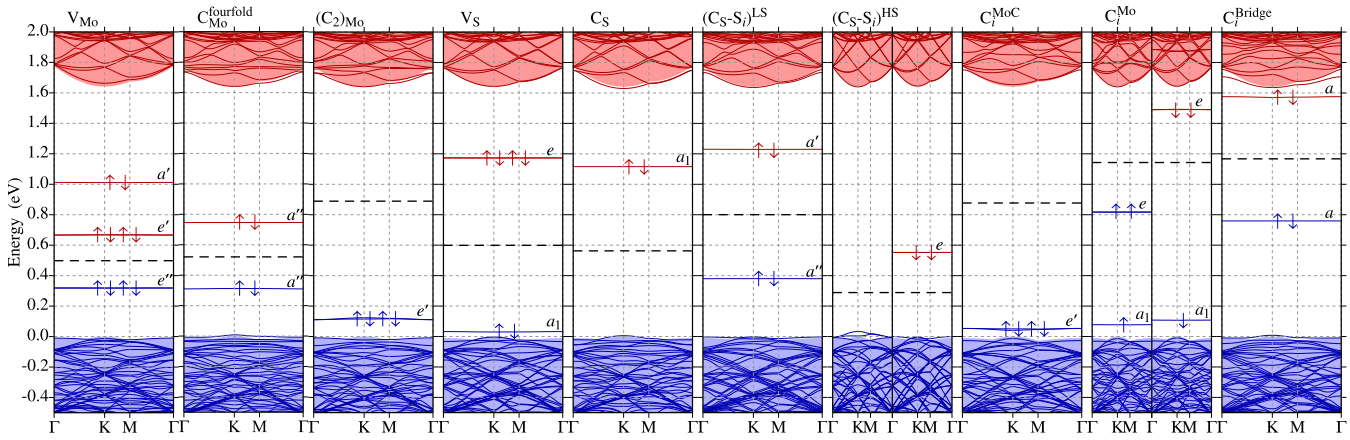


FIG. 3. Electronic band structure in the vicinity of the band gap for selected defects in monolayer MoS_2. Occupied (empty) bands are shown in blue (red), with shading showing envelopes of the defect-free valence and conduction bands. A dividing line halfway between the highest-occupied and lowest-empty state is included for each defect as a horizontal dashed line. Zero on the energy scale is at the valence band maximum. Band structures are spin-averaged except for $(C_S - S_i)^{HS}$ and C_i^{Mo} which are spin triplets, with left and right panels showing up and down spin channels, respectively. Gap-state labels show irreducible representations at Γ. Spin-character and degeneracy of the local occupied and empty states are depicted with up and down arrows irrespective of occupancy. V_{Mo} and V_S have been included for comparison.

process. Even for C_i^{MoC}, with a barrier of around 1.1 eV the process is expected to be rapid enough for this configuration to be considered relatively short lived at room temperature. Since the reactions are exothermic by $\gtrsim$1.7 eV (Table II), reverse reactions are energetically unfavorable. Thus, despite its conceptual distinction from C_i, $C_S - S_i$ is the equilibrium configuration for carbon interstitial point defects, and we conclude that all C_i configurations are expected to be short-lived metastable forms. Unless the complexes and substitutional centers are able to diffuse as units, these are the point defects that are amongst the candidates most likely to be present in sufficient concentrations for observation by spectroscopic means. Since $(C_2)_{Mo}$ is four times more strongly bound than $C_S - S_i$, we suggest a focus should therefore be upon the carbon pair.

One may consider C_S formation from V_S via the interim formation of $C_S - S_i$:

$$V_S + C_i \rightarrow V_S + C_S - S_i \rightarrow V_S + C_S + S_i \rightarrow C_S.$$

This route involves S_i diffusion as opposed to C_i, however, since the barrier to dissociation of S_i from $C_S - S_i$ is 3.4 eV it is unlikely to occur, whereas the reverse barrier (i.e., the barrier to sulfur binding to $C_S - S_i$) is 1.8 eV.

C. Electronic structures

Next we turn to the electronic structure, depicted in Fig. 3, and initially focus upon substitutional centers. Defect-induced band-gap states may act as carrier sources and/or traps, optical transition mechanisms, and carrier scattering centers in devices and hence impact optoelectronic performance. The vacancy band structures shown in Fig. 3 provide benchmark data and are in good agreement with the literature [24,25,80,81], giving confidence to our calculated electronic structures.

C_{Mo} and $(C_2)_{Mo}$ both give rise to deep gap-states. The unsaturated S-sites in C_{Mo}, just as with V_{Mo}, result in both occupied and empty states, whereas the fully bonded $(C_2)_{Mo}$ only results in occupied states in the vicinity of the valence band maximum E_{VBM}. The relatively low symmetry of C_{Mo} and fewer unsaturated sites mean that there are fewer gap states than V_{Mo}. The presence of both occupied and empty states in the gap for C_{Mo} also gives rise to the potential of an optical transition. Based upon the band structure, the zero phonon optical absorption energies would be around 0.5 eV, rendering it in the near infrared. In contrast, the band structure of $(C_2)_{Mo}$ suggests it to be electrically inactive, and although transitions involving localized states resonant with the host bands cannot be ruled out, it seems unlikely $(C_2)_{Mo}$ would give rise to sharp optical transitions, there being only occupied levels very close to the E_{VBM}.

C_S, amongst other carbon-containing centers, has been suggested to lead to *p*-type doping [37]. Figure 3 shows a single localized, unoccupied state lying above mid-gap. This is also what is seen in the band diagrams in Refs. [37,47]. However, the gap state is self-evidently a deep acceptor level, inconsistent with the assertion that C_S could be responsible for *p*-type conduction.

To address the question of *p*-type doping, first and second acceptor levels of all investigated substitutional and interstitial centers have been estimated using the FNV charge correction scheme (Sec. II). Only $(C_S - S_i)^{HS}$, C_S and C_{Mo} present as candidates for single acceptors/electron traps with acceptor levels 1.0, 1.3, and 1.1 eV above the VBM, respectively. These represent deep levels, therefore incompatible with considerable electrical doping at room temperature [37]. No carbon-containing centers are found to have second acceptor levels within the band gap.

Next, we review the electronic structure of the interstitial centers, which includes nonequilibrium arrangements for comparison with the literature. All structures examined give rise to gap levels. The pair of filled states close to the valence band edge for C_i^{MoC} are also reported in Ref. [51]. The gap states of C_i^{Mo} and C_i^{Bridge} are also in agreement with the literature [37,47,51].

TABLE IV. Formation energies, E_f, for configurations in the neutral, +1 and +2 charge states of C_i and $C_S - S_i$. (1/0) and (2/1) denotes the thermal single and double donor levels, respectively, with (2/0) being the transition directly between +2 and neutral charge states. Donor levels are quoted relative to the valence band maximum in eV, with positive values being above the valence band maximum. The corresponding energy from the conduction band minimum is equal to the 1.6 eV minus the donor value in each case. Formation energies for charged systems are expressed as $C + q\Delta\mu_e$ where $\Delta\mu_e = 0$ for $\mu_e = E_{VBM}$. The energies and transitions marked † result from the relaxation from the C_i^{Bridge} structure in the +1 charge state to a perturbed form of $C_S - S_i$ in the +2 charge state. See Ref. [74] for details.

	E_f			Donor levels		
Defect	$q=0$	$q=1$	$q=2$	(1/0)	(2/1)	(2/0)
$(C_S - S_i)^{LS}$	3.1	$3.1 + \Delta\mu_e$	$4.0 + 2\Delta\mu_e$	+0.0	−1.1	−0.5
$(C_S - S_i)^{HS}$	3.1	$3.4 + \Delta\mu_e$	$4.2 + 2\Delta\mu_e$	−0.3	−0.9	−0.6
C_i^{MoC}	4.7	$5.0 + \Delta\mu_e$	$5.9 + 2\Delta\mu_e$	−0.3	−0.9	−0.6
C_i^{Mo}	5.1	$4.7 + \Delta\mu_e$	$5.0 + 2\Delta\mu_e$	+0.4	−0.3	+0.1
C_i^{Bridge}	5.2	$4.5 + \Delta\mu_e$	$4.3^{\dagger} + 2\Delta\mu_e$	+0.7	$+0.2^{\dagger}$	$+0.5^{\dagger}$

The fact that there is only one pair of occupied, degenerate bands for C_i^{MoC} close to E_{VBM} is consistent with this being a low energy structure, with other higher energy forms of C_i, including C_i^{v} and C_i^{S} (see supplemental information for C_i^{v} and C_i^{S} band structures), possessing bands deep in the band gap. The equilibrium interstitial structure, in contrast to the other arrangements, does not present obvious optical transition mechanisms, other than those involving the underlying MoS_2 bands, such as photo-ionization.

$C_S - S_i$ is compositionally identical to C_i, but significantly lower in energy. The spin singlet and triplet states have different structures and correspondingly different band structures. These centers are more favorable than C_i and therefore more likely to be observed in experiment. Based upon occupancy, electron-spin conservation, and dipole selection rules, there are transition mechanisms for the spin-singlet form, $(C_S - S_i)^{LS}$. Based purely upon the band structure, the zero phonon optical absorption energies for these systems would be around 0.9 eV, being in the near infrared range. The spin-triplet band structure does not indicate an inter-level transition, and neither form is an obvious candidate for releasing either electrons or holes to generate electrical conduction.

In addition to the band-structure, to further address the possibility of charge transition levels leading to *n*-type conductivity, the thermal ionization energies of C_i and $C_S - S_i$ have been estimated using the FNV correction approach (Sec. II). The results are presented in Table IV, which shows the donor levels, where they exist, are deep in the gap. Further to this, second-donor levels have also been modeled, and for all the cases analyzed, this level is placed further from the conduction band than the first ionization level. The closest level, either single or double, to the conduction band minimum (E_{CBM}) is for C_i^{Bridge} at $E_{CBM} - 0.9$ eV. This is far too deep for significant thermal ionization at room temperature, and should not be considered as being able to give rise to *n*-type material. Perhaps more significantly, the equilibrium form of interstitial carbon, C_i^{MoC}, does not have a donor level in the band gap, nor does $C_S - S_i$.

Indeed, we conclude that the electronic structures and calculated charge transition levels for all carbon-containing centers examined indicate that it will only act as a deep carrier trap, suggesting it would impede electrical conduction in the absence of other components (such as hydrogen [46]).

D. Vibrational modes

The final defect properties we have evaluated are the local vibrational modes (LVMs), which are listed in Table V. In the absence of comparative vibrational data for C impurities, we have calculated the vibrational modes of ethanethiol, CH_3CH_2SH to provide a benchmark. C–S and C–C stretch modes are calculated at 647 and 957 cm^{-1}, respectively, compared to 663 and 969 cm^{-1} from experiment [82]. We take this approx. 3% underestimate to be indicative of the level of accuracy of the predicted LVMs listed in Table V.

We note the C–S and C–C stretch modes (ω_5–ω_8) are in the same spectral range as ethanethiol stretch modes. Crucially, all defects investigated possess at least one LVM that would be observable in IR and/or Raman spectroscopy, and when combined with isotopic shifts and polarization, these modes would be expected to provide a high degree of specificity for determining the microstructure. This may be particularly important for C_S, $(C_S - S_i)^{HS}$ and $(C_2)_{Mo}$, as there is little prospect of detecting these centers via electronic transitions due to the absence of optical transition mechanisms in these cases (see Sec. III C).

IV. DISCUSSION AND CONCLUSIONS

An exploration of carbon point defects in monolayer MoS_2 from first principles has been conducted. Impurities at the sulfur and molybdenum sites have been investigated, in addition to the carbon interstitial guided by the proposal that C_i might lead to electrical doping and associated conductivity [37].

The first conclusion we draw is that the literature proposals [32,37,47–49] for the geometry of both C_{Mo} and C_i should be reconsidered. In the case of C_{Mo}, chemical reconstruction to form an approximately tetrahedral arrangement of C–S bonds is 0.6 eV lower in energy than the threefold coordinated structure reported in the literature [32] resulting from an off-site displacement of carbon along [0001]. Localized, occupied Kohn-Sham states and the total charge density are strongly indicative of four C–S covalent bonds, with sp^3 hybridization at the carbon atom. Numerous geometries have been proposed in the literature for C_i, predominantly a structure featuring carbon coordinated with sulfur. However, we confirm that the equilibrium interstitial geometry identified in an earlier publication [51] is ∼0.5 eV lower in energy than the commonly reported geometry of C_i^{Mo}. The favorability of C_i^{MoC} suggests both that carbon would be able to move through MoS_2 layers due to its intermediate vertical position in the MoS_2 layer, and that the molybdenum carbide bond formation is energetically favorable despite the apparent limited space to accommodate the carbon interstitial. Critically, none of the C_i centers modeled are realistic candidates for electrical doping of MoS_2, as they give rise to deep donor levels. This strongly counters the suggestion that C_i is responsible for the observed electrical conductivity [37].

TABLE V. Local vibrational modes of carbon defects in monolayer MoS_2, their point-group symmetry and irreducible representations. Local modes are identified as lying above 456 cm^{-1}, the calculated one-phonon maximum. All modes listed are infrared and Raman active except ω_6 which is Raman-inactive and ω_7 and ω_8 which are IR-inactive. Wave numbers are provided for ^{12}C, with the shift to lower wave number for ^{13}C shown in parentheses. For $(C_2)_{Mo}$, the two shifts correspond to first the mixed-isotope case and then ^{13}C, with the mixed-isotope case possessing C_{3v} symmetry.

Defect	Label	Sym.	Wave number	Description of predominant mode contributions
C_S	ω_0	C_{3v}, A_1	578(19)	C–Mo–S bend/scissor.
	ω_1	C_{3v}, E	638(23)	C–Mo stretch.
C_{Mo}	ω_2	C_{1h}, A''	641(32)	C–S stretch in MoS_2 plane.
	ω_3	C_{1h}, A'	680(22)	C–S stretch in MoS_2 plane.
	ω_4	C_{1h}, A'	722(24)	C–S stretch normal to MoS_2 plane.
$(C_2)_{Mo}$	ω_5	D_{3h}, E'	675(13, 22)	In-phase stretch of two C–S.
	ω_6	D_{3h}, A_2'	693(11, 20)	In-phase bending of all C–S bonds.
	ω_7	D_{3h}, E''	782(13, 29)	The corresponding anti-phase C–S stretch to ω_5.
	ω_8	D_{3h}, A_1'	935(17, 36)	C–C stretch.
$(C_S - S_i)^{HS}$	ω_{10}	C_{3v}, A_1	971(29)	C–S_i stretch.
$(C_S - S_i)^{LS}$	ω_{11}	C_{1h}, A'	499(18)	C–Mo stretch.
	ω_{12}	C_{1h}, A''	540(19)	Anti-phase stretch of two C–Mo.
	ω_{13}	C_{1h}, A'	971(31)	C–S_i stretch.

Indeed, it is not plausible from our data to conceive that any of the carbon or native defects modeled here are likely to be a source of free carriers, and therefore they are unable to account for the evolution from *p*-type to *n*-type by the addition of carbon as suggested previously [37]. In particular, sulfur vacancies are deep acceptors and are unable to introduce holes to the valence band under ambient conditions. Interstitial carbon in any of the many forms reviewed, including the compositionally identical $C_S - S_i$, possesses only deep donor levels, if any at all, and is therefore unable to introduce electrons to the conduction band under ambient conditions. We conclude that the experimental observations of *n*-type conduction [37] remain entirely unexplained by carbon or monovacancy defects, although the observed nanometer-scale carbon clusters are yet to be investigated.

The second area of focus is the identification of two novel stable structures, $(C_2)_{Mo}$ and $C_S - S_i$, which to our knowledge, have not previously been considered. These centers represent the energetically favorable carbon-containing point defects at the molybdenum and sulfur sites, respectively. Even more importantly, $C_S - S_i$ is thermally accessible via rearrangement from all the considered C_i configurations, so we consider it more appropriate to regard $C_S - S_i$ as the equilibrium C_i arrangement, where carbon occupies a substitutional site, rather than carbon existing as an interstitial in MoS_2. As with C_{Mo}, the orbitals and charge density support assignment of C–S covalent bonding between these species, with single and double bonds forming in $(C_2)_{Mo}$ and $C_S - S_i$, respectively.

Thirdly, when considering the centers likely to be present in MoS_2 when contaminated by carbon, we focus upon the formation energies in the Mo- and S-rich limits. $C_S - S_i$ and $(C_2)_{Mo}$ are energetically most favorable under S-rich growth conditions, whereas under Mo-rich conditions, the most favorable carbon point defect is C_S. As one might expect and as illustrated by the low-energy configurations identified here, configurations broadly become more energetically favorable with the reduction in the number of under-coordinated sites in the cases of substitutional carbon. Such coordination arguments, whilst generally helpful, do not readily explain the relative energies among C_i configurations, for which factors including over-coordination of neighboring host atoms and charge redistribution are likely contributions to both the relatively high formation energies and the variations in energy with C_i configuration. Indeed, we note that across the range of carbon-centers of all types, gap-states exhibit contributions from Mo–Mo *d*–*d* bonding (see Ref. [74]). The contribution from such interactions would be of interest in a detailed exploration of the chemistry, a potential subject for future study.

Finally, we have provided vibrational wave numbers for local modes that give a potential route to unambiguous identification of the microstructures of carbon-containing defects in MoS_2. The direct, spectroscopic identification of carbon microstructure is critical to resolving what, if any, role carbon point defects have on the production of *n*-type conduction in MoS_2.

In summary, we present an expanded picture of carbon impurities in monolayer MoS_2, increasing not only the breadth of defects considered, but also the amount of derived quantities and observables. These data are intended to facilitate the experimental exploration of carbon impurities.

ACKNOWLEDGMENTS

The authors acknowledge the Engineering and Physical Sciences Research Council (EPSRC) Centre for Doctoral training in Renewable Energy Northeast Universities (ReNU) for funding through Grant No. EP/S023836/1. F.A. and J.G. are also grateful to the Deanship of Graduate Studies and Scientific Research at Najran University for funding this work under the SAFEER Funding Program (grant code: NU/SAFEER/SERC/14/3418-1).

DATA AVAILABILITY

The data that support the findings of this article are not publicly available. The data are available from the authors upon reasonable request.

[1] K. S. Novoselov, A. K. Geim, S. V. Morozov, D. Jiang, Y. Zhang, S. V. Dubonos, I. V. Grigorieva, and A. A. Firsov, Electric field effect in atomically thin carbon films, Science **306**, 666 (2004).

[2] D. Frank, R. Dennard, E. Nowak, P. Solomon, Y. Taur, and H.-S. P. Wong, Device scaling limits of Si MOSFETs and their application dependencies, Proc. IEEE **89**, 259 (2001).

[3] W. T. Cong, Z. Tang, X. G. Zhao, and J. H. Chu, Enhanced magnetic anisotropies of single transition-metal adatoms on a defective MoS_2 monolayer, Sci. Rep. **5**, 9361 (2015).

[4] C. Li, Q. Cao, F. Wang, Y. Xiao, Y. Li, J.-J. Delaunay, and H. Zhu, Engineering graphene and TMDs based van der waals heterostructures for photovoltaic and photoelectrochemical solar energy conversion, Chem. Soc. Rev. **47**, 4981 (2018).

[5] Y. Yin, Z. Zhang, C. Shao, J. Robertson, and Y. Guo, Computational study of transition metal dichalcogenide cold source MOSFETs with sub-60 mV per decade and negative differential resistance effect, npj 2D Mat. and Appl. **6**, 55 (2022).

[6] B. Radisavljevic, M. B. Whitwick, and A. Kis, Integrated circuits and logic operations based on single-layer MoS_2, ACS Nano **5**, 9934 (2011).

[7] D. Jariwala, V. K. Sangwan, L. J. Lauhon, T. J. Marks, and M. C. Hersam, Emerging device applications for semiconducting two-dimensional transition metal dichalcogenides, ACS Nano **8**, 1102 (2014).

[8] C. R. Ryder, J. D. Wood, S. A. Wells, and M. C. Hersam, Chemically tailoring semiconducting two-dimensional transition metal dichalcogenides and black phosphorus, ACS Nano **10**, 3900 (2016).

[9] K. K. Kam and B. A. Parkinson, Detailed photocurrent spectroscopy of the semiconducting group VI transition metal dichalcogenides, J. Phys. C **86**, 463 (1982).

[10] J. Gusakova, X. Wang, L. L. Shiau, A. Krivosheeva, V. Shaposhnikov, V. Borisenko, V. Gusakov, and B. K. Tay, Electronic properties of bulk and monolayer TMDs: Theoretical study within DFT framework (GVJ-2E method), Phys. Status Solidi (a) **214**, 1700218 (2017).

[11] K. F. Mak, C. Lee, J. Hone, J. Shan, and T. F. Heinz, Atomically thin MoS_2: A new direct-gap semiconductor, Phys. Rev. Lett. **105**, 136805 (2010).

[12] J. O. Island, A. Kuc, E. H. Diependaal, R. Bratschitsch, H. S. van der Zant, T. Heine, and A. Castellanos-Gomez, Precise and reversible band gap tuning in single-layer $MoSe_2$ by uniaxial strain, Nanoscale **8**, 2589 (2016).

[13] Y. L. Huang, Y. Chen, W. Zhang, S. Y. Quek, C.-H. Chen, L.-J. Li, W.-T. Hsu, W.-H. Chang, Y. J. Zheng, W. Chen, and A. T. S. Wee, Bandgap tunability at single-layer molybdenum disulphide grain boundaries, Nat. Commun. **6**, 6298 (2015).

[14] B. Radisavljevic, A. Radenovic, J. Brivio, V. Giacometti, and A. Kis, Single-layer MoS_2 transistors, Nat. Nanotechnol. **6**, 147 (2011).

[15] A. Castellanos-Gomez, M. Poot, G. A. Steele, H. S. van der Zant, N. Agraït, and G. Rubio-Bollinger, Elastic properties of freely suspended MoS_2 nanosheets, Adv. Mater. **24**, 772 (2012).

[16] M. Bernardi, M. Palummo, and J. C. Grossman, Extraordinary sunlight absorption and one nanometer thick photovoltaics using two-dimensional monolayer materials, Nano Lett. **13**, 3664 (2013).

[17] D. Jariwala, A. R. Davoyan, J. Wong, and H. A. Atwater, van der Waals materials for atomically-thin photovoltaics: Promise and outlook, ACS Photon. **4**, 2962 (2017).

[18] K.-H. Kim, M. Andreev, S. Choi, J. Shim, H. Ahn, J. Lynch, T. Lee, J. Lee, K. N. Nazif, A. Kumar, P. Kumar, H. Choo, D. Jariwala, K. C. Saraswat, and J.-H. Park, High-efficiency WSe_2 photovoltaic devices with electron-selective contacts, ACS Nano **16**, 8827 (2022).

[19] M. Tsai, M. Li, J. R. Retamal, K. Lam, Y. Lin, K. Suenaga, L. Chen, G. Liang, L. Li, and J. He, Single atomically sharp lateral monolayer p-n heterojunction solar cells with extraordinarily high power conversion efficiency, Adv. Mater. **29**, 1701168 (2017).

[20] D. Kwak, H. Ra, M. Jeong, A. Lee, and J. Lee, High-performance photovoltaic effect with electrically balanced charge carriers in black phosphorus and WS_2 heterojunction, Adv. Mater. Interfaces **5**, 1800671 (2018).

[21] K. Nassiri Nazif, A. Daus, J. Hong, N. Lee, S. Vaziri, A. Kumar, F. Nitta, M. E. Chen, S. Kananian, R. Islam, K.-H. Kim, J.-H. Park, A. S. Y. Poon, M. L. Brongersma, E. Pop, and K. C. Saraswat, High-specific-power flexible transition metal dichalcogenide solar cells, Nat. Commun. **12**, 7034 (2021).

[22] S. Tongay, J. Suh, C. Ataca, W. Fan, A. Luce, J. S. Kang, J. Liu, C. Ko, R. Raghunathanan, J. Zhou, F. Ogletree, J. Li, J. C. Grossman, and J. Wu, Defects activated photoluminescence in two-dimensional semiconductors: Interplay between bound, charged and free excitons, Sci. Rep. **3**, 2657 (2013).

[23] K. Nassiri Nazif, A. Kumar, J. Hong, N. Lee, R. Islam, C. J. McClellan, O. Karni, J. van de Groep, T. F. Heinz, E. Pop, M. L. Brongersma, and K. C. Saraswat, High-performance p-n junction transition metal dichalcogenide photovoltaic cells enabled by MoO_x doping and passivation, Nano Lett. **21**, 3443 (2021).

[24] W. Zhou, X. Zou, S. Najmaei, Z. Liu, Y. Shi, J. Kong, J. Lou, P. M. Ajayan, B. I. Yakobson, and J.-C. Idrobo, Intrinsic structural defects in monolayer molybdenum disulfide, Nano Lett. **13**, 2615 (2013).

[25] Q. Xu, G. Yang, and W. Zheng, DFT calculation for stability and quantum capacitance of MoS_2 monolayer-based electrode materials, Mater. Today Commun. **22**, 100772 (2020).

[26] A. M. Z. Tan, C. Freysoldt, and R. G. Hennig, Stability of charged sulfur vacancies in 2D and bulk MoS_2 from plane-wave density functional theory with electrostatic corrections, Phys. Rev. Mater. **4**, 064004 (2020).

[27] S. Haldar, H. Vovusha, M. K. Yadav, O. Eriksson, and B. Sanyal, Systematic study of structural, electronic, and optical properties of atomic-scale defects in the two-dimensional transition metal dichalcogenides, Phys. Rev. B **92**, 235408 (2015).

[28] H.-P. Komsa and A. V. Krasheninnikov, Native defects in bulk and monolayer MoS_2 from first principles, Phys. Rev. B **91**, 125304 (2015).

[29] J.-Y. Noh, H. Kim, and Y.-S. Kim, Stability and electronic structures of native defects in single-layer MoS_2, Phys. Rev. B **89**, 205417 (2014).

[30] V. Gusakov, J. Gusakova, and B. K. Tay, Formation and diffusion of intrinsic point defects in bulk and monolayer MoS_2: First-principles study, Phys. Status Solidi (b) **259**, 2100479 (2022).

[31] S. Kc, R. C. Longo, R. Addou, R. M. Wallace, and K. Cho, Impact of intrinsic atomic defects on the electronic structure of MoS_2 monolayers, Nanotechnology **25**, 375703 (2014).

[32] T. Liang, M. R. Habib, H. Xiao, S. Xie, Y. Kong, C. Yu, H. Iwai, D. Fujita, N. Hanagata, H. Chen, Z. Feng, and M. Xu, Intrinsically substitutional carbon doping in CVD-grown monolayer MoS_2 and the band structure modulation, ACS Appl. Electron. Mater. **2**, 1055 (2020).

[33] C. M. Schaefer, J. M. Caicedo Roque, G. Sauthier, J. Bousquet, C. Hébert, J. R. Sperling, A. Pérez-Tomás, J. Santiso, E. del Corro, and J. A. Garrido, Carbon incorporation in MOCVD of MoS_2 thin films grown from an organosulfide precursor, Chem. Mater. **33**, 4474 (2021).

[34] A. Ghiami, A. Grundmann, S. Tang, H. Fiadziushkin, Z. Wang, S. Aussen, S. Hoffmann-Eifert, M. Heuken, H. Kalisch, and A. Vescan, Impact of carbon impurities on air stability of MOCVD 2D-MoS_2, Surfaces **6**, 351 (2023).

[35] T. Hou, D. Li, Y. Qu, Y. Hao, and Y. Lai, The role of carbon in metal–organic chemical vapor deposition-grown MoS_2 films, Materials **16**, 7030 (2023).

[36] S. Park, S. Siahrostami, J. Park, A. H. B. Mostaghimi, T. R. Kim, L. Vallez, T. M. Gill, W. Park, K. E. Goodson, R. Sinclair, and X. Zheng, Effect of adventitious carbon on pit formation of monolayer MoS_2, Adv. Mater. **32**, 2003020 (2020).

[37] Y. Park, N. Li, D. Jung, L. T. Singh, J. Baik, E. Lee, D. Oh, Y. D. Kim, J. Y. Lee, J. Woo, S. Park, H. Kim, G. Lee, G. Lee, and C.-C. Hwang, Unveiling the origin of n-type doping of natural MoS_2: Carbon, npj 2D Mater. Appl. **7**, 60 (2023).

[38] S. Kim, A. Konar, W.-S. Hwang, J. H. Lee, J. Lee, J. Yang, C. Jung, H. Kim, J.-B. Yoo, J.-Y. Choi, Y. W. Jin, S. Y. Lee, D. Jena, W. Choi, and K. Kim, High-mobility and low-power thin-film transistors based on multilayer MoS_2 crystals, Nat. Commun. **3**, 1011 (2012).

[39] Z. Yin, H. Li, H. Li, L. Jiang, Y. Shi, Y. Sun, G. Lu, Q. Zhang, X. Chen, and H. Zhang, Single-layer MoS_2 phototransistors, ACS Nano **6**, 74 (2011).

[40] H. Schmidt, S. Wang, L. Chu, M. Toh, R. Kumar, W. Zhao, A. H. Castro Neto, J. Martin, S. Adam, B. Özyilmaz, and G. Eda, Transport properties of monolayer MoS_2 grown by chemical vapor deposition, Nano Lett. **14**, 1909 (2014).

[41] H. Li, Z. Yin, Q. He, H. Li, X. Huang, G. Lu, D. W. Fam, A. I. Tok, Q. Zhang, and H. Zhang, Fabrication of single- and multilayer MoS_2 film-based field-effect transistors for sensing no at room temperature, Small **8**, 63 (2011).

[42] Y.-H. Lee, X.-Q. Zhang, W. Zhang, M.-T. Chang, C.-T. Lin, K.-D. Chang, Y.-C. Yu, J. T.-W. Wang, C.-S. Chang, L.-J. Li, and T.-W. Lin, Synthesis of large-area MoS_2 atomic layers with chemical vapor deposition, Adv. Mat. **24**, 2320 (2012).

[43] K.-K. Liu, W. Zhang, Y.-H. Lee, Y.-C. Lin, M.-T. Chang, C.-Y. Su, C.-S. Chang, H. Li, Y. Shi, H. Zhang, C.-S. Lai, and L.-J. Li, Growth of large-area and highly crystalline MoS_2 thin layers on insulating substrates, Nano Lett. **12**, 1538 (2012).

[44] B. W. Baugher, H. O. Churchill, Y. Yang, and P. Jarillo-Herrero, Intrinsic electronic transport properties of high-quality monolayer and bilayer MoS_2, Nano Lett. **13**, 4212 (2013).

[45] J.-H. Ahn, W. M. Parkin, C. H. Naylor, A. T. Johnson, and M. Drndić, Ambient effects on electrical characteristics of CVD-grown monolayer MoS_2 field-effect transistors, Sci. Rep. **7**, 4075 (2017).

[46] A. Singh and A. K. Singh, Origin of *n*-type conductivity of monolayer MoS_2, Phys. Rev. B **99**, 121201(R) (2019).

[47] A. K. Auni, J. Manopo, I. S. Sianturi, A. Hadju, A. L. Ivansyah, Y. Darma, and F. Muttaqien, An *ab initio* study of carbon impurities on single-layer MoS_2 for optoelectronic applications, ACS Appl. Nano Mat. **7**, 28098 (2024).

[48] J. He, K. Wu, R. Sa, Q. Li, and Y. Wei, Magnetic properties of nonmetal atoms absorbed MoS_2 monolayers, Appl. Phys. Lett. **96**, 082504 (2010).

[49] X. D. Li, Y. M. Fang, S. Q. Wu, and Z. Z. Zhu, Adsorption of alkali, alkaline-earth, simple and 3D transition metal, and nonmetal atoms on monolayer MoS_2, AIP Adv. **5**, 082504 (2015).

[50] M. Aghajanian, A. A. Mostofi, and J. Lischner, Tuning electronic properties of transition-metal dichalcogenides via defect charge, Sci. Rep. **8**, 13611 (2018).

[51] C. Ataca and S. Ciraci, Functionalization of single-layer MoS_2 honeycomb structures, J. Phys. Chem. C **115**, 13303 (2011).

[52] M. J. Rayson and P. R. Briddon, Highly efficient method for kohn-sham density functional calculations of 500-10000 atom systems, Phys. Rev. B **80**, 205104 (2009).

[53] R. Jones and P. R. Briddon, The *ab initio* cluster method and the dynamics of defects in semiconductors, Semicond. Semimet. **51**, 287 (1998).

[54] J. P. Perdew, K. Burke, and M. Ernzerhof, Generalized gradient approximation made simple, Phys. Rev. Lett. **77**, 3865 (1996).

[55] S. Grimme, Semiempirical GGA-type density functional constructed with a long-range dispersion correction, J. Comput. Chem. **27**, 1787 (2006).

[56] D. Kieczka, T. Durrant, K. Milton, K. E. J. Goh, M. Bosman, and A. Shluger, Defects in WS_2 monolayer calculated with a nonlocal functional: Any difference from GGA? Electron. Struct. **5**, 024001 (2023).

[57] M. H. Naik and M. Jain, Substrate screening effects on the quasiparticle band gap and defect charge transition levels in MoS_2, Phys. Rev. Mater. **2**, 084002 (2018).

[58] C. Hartwigsen, S. Goedecker, and J. Hutter, Relativistic separable dual-space Gaussian pseudopotentials from H to Rn, Phys. Rev. B **58**, 3641 (1998).

[59] M. Krack, Pseudopotentials for H to Kr optimized for gradient-corrected exchange-correlation functionals, Theor. Chem. Acc. **114**, 145 (2005).

[60] J. P. Goss, M. J. Shaw, and P. R. Briddon, Marker-method calculations for electrical levels using Gaussian-orbital basis sets, in *Theory of Defects in Semiconductors*, Topics in Applied Physics, Vol. 104, edited by D. A. Drabold and S. K. Estreicher (Springer, Berlin, Heidelberg, 2007), pp. 69–94.

[61] H. J. Monkhorst and J. D. Pack, Special points for Brillouin-zone integrations, Phys. Rev. B **13**, 5188 (1976).

[62] O. K. Le, V. Chihaia, M.-P. Pham-Ho, and D. N. Son, Electronic and optical properties of monolayer MoS_2 under the influence of polyethyleneimine adsorption and pressure, Royal Soc. Chem. Adv. **10**, 4201 (2020).

[63] C. Ataca, H. Sahin, E. Akturk, and S. Ciraci, Mechanical and electronic properties of MoS_2 nanoribbons and their defects, J. Phys. Chem. C **115**, 3934 (2011).

[64] N. N. Hieu, V. V. Ilyasov, T. V. Vu, N. A. Poklonski, H. V. Phuc, L. T. Phuong, B. D. Hoi, and C. V. Nguyen, First principles study of optical properties of molybdenum disulfide: From bulk to monolayer, Superlattices Microstruct. **115**, 10 (2018).

[65] C. Freysoldt, J. Neugebauer, and C. G. Van de Walle, Electrostatic interactions between charged defects in supercells, Phys. Status Solidi (b) **248**, 1067 (2011).

[66] C. Freysoldt, J. Neugebauer, and C. G. Van de Walle, Fully *ab initio* finite-size corrections for charged-defect supercell calculations, Phys. Rev. Lett. **102**, 016402 (2009).

[67] C. Freysoldt and J. Neugebauer, First-principles calculations for charged defects at surfaces, interfaces, and two-dimensional materials in the presence of electric fields, Phys. Rev. B **97**, 205425 (2018).

[68] J. Y. Kim, l. Gelczuk, M. P. Polak, D. Hlushchenko, D. Morgan, R. Kudrawiec, and I. Szlufarska, Experimental and theoretical studies of native deep-level defects in transition metal dichalcogenides, npj 2D Mater. Appl. **6**, 75 (2022).

[69] F. Goto, Cohesive energy of diamond, J. Phys. Soc. Jpn. **21**, 895 (1966).

[70] A. G. Gaydon and W. G. Penney, The dissociation energies of CO, N_2, NO and CN, Proc. R. Soc. London, Ser. A **183**, 374 (1945).

[71] G. Henkelman, B. P. Uberuaga, and H. Jónsson, A climbing image nudged elastic band method for finding saddle points and minimum energy paths, J. Chem. Phys. **113**, 9901 (2000).

[72] G. Henkelman and H. Jónsson, Improved tangent estimate in the nudged elastic band method for finding minimum energy paths and saddle points, J. Chem. Phys. **113**, 9978 (2000).

[73] R. Jones, J. Goss, C. Ewels, and S. Öberg, *Ab initio* calculations of anharmonicity of the C–H stretch mode in HCN and GaAs, Phys. Rev. B **50**, 8378 (1994).

[74] See Supplemental Material at http://link.aps.org/supplemental/10.1103/wfjb-8dd2 for additional plan-view schematic illustrations of the defects, and additional data.

[75] K. KuO and G. Hägg, A new molybdenum carbide, Nature (London) **170**, 245 (1952).

[76] Y. J. Cho, Y. Sim, J.-H. Lee, N. T. Hoang, and M.-J. Seong, Size and shape control of CVD-Grown monolayer MoS_2, Curr. Appl. Phys. **45**, 99 (2023).

[77] D. Zhu, H. Shu, F. Jiang, D. Lv, V. Asokan, O. Omar, J. Yuan, Z. Zhang, and C. Jin, Capture the growth kinetics of CVD growth of two-dimensional MoS_2, npj 2D Mater. Appl. **1**, 8 (2017).

[78] J. Yue, J. Jian, P. Dong, L. Luo, and F. Chang, Growth of single-layer MoS_2 by chemical vapor deposition on sapphire substrate, IOP Mater. Sci. Eng. **592**, 012044 (2019).

[79] L. Brewer, Cohesive energies of the elements, Tech. Rep. LBL-3720 (Lawrence Berkeley National Lab. (LBNL), Berkeley, CA, USA, 1975).

[80] L.-p. Feng, J. Su, and Z.-t. Liu, Effect of vacancies on structural, electronic and optical properties of monolayer MoS_2: A first-principles study, J. Appl. Cryst. **613**, 122 (2014).

[81] L.-p. Feng, H.-q. Sun, A. Li, J. Su, Y. Zhang, and Z.-t. Liu, Influence of Mo-vacancy concentration on the structural, electronic and optical properties of monolayer MoS_2: A first-principles study, Mater. Chem. Phys. **209**, 146 (2018).

[82] H. Wolff and J. Szydlowski, Vibrational spectra and rotational isomerism of ethanethiol and ethanethiol-D1, Can. J. Chem. **63**, 1708 (1985).